Epitaxy enhancement in oxide/tungsten heterostructures by harnessing the interface adhesion

Anna L. Ravensburg[1] · Rimantas Brucas[2] · Denis Music[3,4] · Lennart Spode[1] · Gunnar K. Pálsson[1] · Peter Svedlindh[2] · Vassilios Kapaklis[1]

Abstract

The conditions whereby epitaxy is achieved are commonly believed to be mostly governed by misfit strain. We report on a systematic investigation of growth and interface structure of single crystalline tungsten thin films on two different metal oxide substrates, Al_2O_3 ($11\bar{2}0$) and MgO (001). We demonstrate that despite a significant mismatch, enhanced crystal quality is observed for tungsten grown on the sapphire substrates. This is promoted by stronger adhesion and chemical bonding with sapphire compared to magnesium oxide, along with the restructuring of the tungsten layers close to the interface. The latter is supported by ab initio calculations using density functional theory. Finally, we demonstrate the growth of magnetic heterostructures consisting of high-quality tungsten layers in combination with ferromagnetic CoFe layers, which are relevant for spintronic applications.

Keywords Epitaxy · Interface · Crystal structure · Scattering

1 Introduction

Spintronic devices, consisting of ferromagnetic layers separated by a nonmagnetic metal or an insulating layer, use spin-dependent electron transport to detect changes in magnetic fields [1]. In light of this, heterostructures of ferromagnetic layers in proximity to $4d$ and $5d$ non-magnetic metals are of particular interest. For example, such heterostructures can be used to tune the strength and type of interlayer exchange coupling in trilayers and to fine-tune the magnetization dynamics [2, 3]. Most of these heterostructures have to be grown on oxide substrates, making the oxide/metal interface with its chemistry and structure on multiple length scales an important parameter to consider while designing and evaluating the performance of a device.

Spin-orbit torques (SOTs) in heavy metal/ferromagnetic heterostructures are gaining increasing attention for providing an efficient pathway for manipulating the free layer magnetization in magnetic random-access memories. The origin of the SOT is the pure spin current J_s generated by a charge current J_c in the heavy metal via the spin-orbit coupling. The charge-to-spin current conversion efficiency can be described by the spin Hall angle $\theta_{SHE} = J_s/J_c$ [4]. Tungsten has, in this respect, been in focus due to large reported values of θ_{SHE} of around -0.3 to -0.4. An equally important parameter for spintronic applications is the transparency of the heavy metal/ferromagnet interface which is controlled by the effective spin-mixing conductance of the interface [5]. The effective spin-mixing conductance describes the transfer of spin current through the interface and also accounts for spin-backflow as well as spin-memory loss at the interface, emphasizing that the interface quality is a critical parameter for spintronic devices. Furthermore, W has been the subject of investigations as fusion reactor plasma-facing material due to its combination of high atomic number and relatively low activation decay time [6, 7]. For these applications, being able to grow well defined crystals of these metals and performing interface engineering is of the outmost

✉ Anna L. Ravensburg
     anna.ravensburg@physics.uu.se

1   Department of Physics and Astronomy, Uppsala University, Box 516, 75120 Uppsala, Sweden

2   Department of Materials Science and Engineering, Uppsala University, Box 35, 75103 Uppsala, Sweden

3   Department of Materials Science and Applied Mathematics, Malmö University, 20506 Malmö, Sweden

4   Biofilms Research Center for Biointerfaces, Malmö University, 20506 Malmö, Sweden

importance; in particular for a potential new generation of spintronic devices where inter-layer spin transport plays an important role.

In thin-film form, besides the ground state bcc α–W phase, tungsten can be stabilized in its β–W phase with an A15 structure [8, 9]. The β-W phase exhibits a large spin Hall angle and therefore also a large charge-to-spin current conversion efficiency, similar to the case of β-Ta [4, 9–11]. The β–W phase growth depends strongly on the deposition conditions during the sputtering process as well as on the film thickness [10, 12, 13]. Thin films may exhibit the β-W phase, while intermediate thicknesses and/or annealing yield mixture of α–W and β–W phase [8, 14]. Thick films tend to be almost pure α–W phase. Furthermore, the majority of these films are polycrystalline forming more complicated interfaces at grain boundaries, with the adjacent substrates, and with additional buffer-layers. Hetero-epitaxial growth of α–W thin films on the other hand, may be enabled through a lattice match between in-plane atomic distances in the film and substrate. The crystal structure of bcc α-W is reported to have a cubic lattice parameter of 3.155 Å [15] to 3.17 Å [16, 17].

Here, we study the sputter growth of highly epitaxial α-W thin films on sapphire, Al_2O_3 ($11\bar{2}0$), and MgO (001) substrates, giving emphasis to the overall quality of the layering and crystal structure. Magnetron sputtering was selected for thin film growth because it offers the best compromise between low defect density and flat layering compared to other physical vapor deposition processes. We further shed more light on interdependencies between the oxide/film interface and the accommodation of the lattice mismatch, with support from ab initio calculations. The Al_2O_3 ($11\bar{2}0$) and MgO (001) substrates were chosen as they are technologically relevant materials, which are used to grow well defined single crystalline metallic layers and, for the case of W growth, offer very different lattice mismatches, which allows for an in-depth study of the epitaxial growth. Another reason for choosing these substrates is that they provide two different interfaces for tungsten; namely W (110) in case of Al_2O_3 ($11\bar{2}0$) and W (001) in case of MgO (001). It has been shown that the W (110) interface exhibits Dirac-type surface states [18], which is believed to have direct impact on spin Hall angle and therefore also on the generation of spin currents. It is therefore motivated to investigate if the two interfaces are different in this respect. In a forthcoming publication we will present results for the generation of THz radiation in W/CoFe bilayers grown on these two substrates. For the case of sapphire substrates, we argue that the interface structure and crystal quality are results of strong adhesion and bonding, similar to the sapphire/Nb system [19, 20]. This system has a well-defined epitaxial relationship at the metal/oxide interface and is thus coordination-specific. Having built a solid foundation for growth

of epitaxial tungsten, we proceed to the growth of epitaxial α–W and ferromagnetic CoFe bilayers. These bilayers are of technological importance, as they might be essential in future spintronic applications, such as THz emitters [21].

2 Methods

2.1 Growth

Thin layers of W and W/CoFe bilayers of different thicknesses were deposited on single crystalline Al_2O_3 ($11\bar{2}0$) and MgO (001) substrates (both 10×10 mm^2) at floating potential, using direct current (dc) and radio frequency (rf) magnetron sputtering. While for the bilayers, first the W and then the CoFe layer were grown on Al_2O_3 ($11\bar{2}0$), the order of the layers was turned around for bilayers grown on MgO (001) due to better lattice matching of CoFe on MgO. Prior to deposition, the substrates were cleaned in acetone and 2-propanol using ultrasonic agitation for 120 s. This was followed by annealing in vacuum at 873(2) K for 3600 s. The base pressure of the growth chamber was below 5×10^{-7} Pa. To prevent surface oxidation of the films, the samples were capped at ambient temperature (< 313(2) K) with Al; selected samples were capped with Al_2O_3 instead. The depositions were carried out in an Ar atmosphere (gas purity $\geq$ 99.999 %, and a secondary getter based purification) from elemental W (25 W, dc) and Al (50 W, dc) targets, and CoFe (13 W, dc) and Al_2O_3 (90 W, rf) compound targets. The targets were cleaned by sputtering against closed shutters for at least 60 s prior to each deposition. The target-to-substrate distance in the deposition chamber was around 0.2 m. The deposition rates (W: 0.23 Å/s, Al: 0.30 Å/s, CoFe: 0.10 Å/s, Al_2O_3: 0.03 Å/s) were calibrated prior to the growth, using x-ray reflectivity. The growth temperatures for each layer and for the bilayers were optimized with respect to layering and crystal quality, yielding 843(2) K for single W layers (one selected sample was grown at 793(2) K instead) and 573(2) K for CoFe layers. For the W/CoFe bilayers, W and CoFe were deposited at 843(2) K and 573(2) K, respectively, if W was grown first, while both layers were deposited at 573(2) K if the CoFe layer was grown first. Finally, to ensure thickness uniformity, the substrate holder was rotated during the deposition.

2.2 Characterization

X-ray reflectometry (XRR) and diffraction (XRD) were carried out in a Bede D1 diffractometer equipped with a Cu K_{α_1} x-ray source operated at 35 mA and 50 kV. A circular mask (diameter: 0.005 m) and an incidence and a detector slit (both 0.0005 m) were used. For monochromatizing the

beam by reducing the CuKβ and CuKα_2 radiation, the setup included a Göbel mirror and a 2-bounce-crystal on the incidence side. The x-rays were detected with a Bede EDRc x-ray detector. The instrument angles were aligned to the sample surface for XRR and to the W crystal planes for XRD measurements. The measured XRR data was fitted using GenX [22, 23] enabling the determination of the scattering length density (SLD) profile which includes information on layer thickness and roughness. However, atomic terraces in the Al$_2$O$_3$ [24] and twinning in the MgO substrates [25], and therefore also in the epitaxial top layers, may lead to an overestimation of the layer roughnesses. In the diffraction experiments, the samples were measured with a combination of coupled 2θ-θ and rocking curve scans. Texture analysis was performed employing rotational ϕ scans at different sample tilts χ. A pole figure was measured for ϕ angles between 350° and 190°. Data in the range between 190° and 350° in ϕ was assumed to be rotational symmetric with an angle of 180°. The lattice mismatch between film and substrate for certain epitaxial relationships was calculated based on a previously established approach by Wildes et al. [20]. Peak positions in 2θ were determined by fitting with a Gaussian function, while rocking curve peaks were fitted with a Lorentzian profile. All error bars for fits of scattering data are statistical and do not include systematic errors arising from alignment or absorption. XRD patterns including Laue oscillations were additionally fitted with GenL [26] enabling the determination of the average number of coherently scattering planes contributing to the Laue oscillations N_L and the average out-of-plane atomic distance of α-W d_{hkl} as well as of a potentially present strain profile and layer/interface roughnesses.

Both, the Hall coefficient and resistivity were measured with a 4-point probe setup in a van der Pauw geometry, with the contact pins placed in the corners of a 8×8 mm^2 square placed concentrically on the sample surface. The film itself had lateral dimensions of 10×9 mm^2. Electronic transport measurements of the resistivity and Hall coefficient were performed during warm-up from 10 to 320 K (resistivity) and 20 to 320 K (Hall coefficient) in a cryostat using a closed cycle He compressor. The temperature was controlled stepwise using a 37 W resistance heater and a Cernox® temperature sensor connected to a LakeShore 340 temperature controller. All measurements were done in thermodynamic equilibrium, by waiting until the temperature and voltage readings stabilised sufficiently for the respective measurements. The resistivity was measured at remanence with reversed polarity measurements [27]. A current of 0.001 A was applied by means of a Keithley 2400 SourceMeter. A Keithley 2182A NanoVoltMeter was used to measure the voltage.

To measure the Hall coefficient, magnetic fields of −0.475 and 0.475 T were applied using a GMW Model 5403 electromagnet and a Kepco BOP 20–50 MG power supply. The magnetic field was measured using a Hall probe and a LakeShore 455 Gaussmeter. The same 4-point probe setup as for the resistivity measurements was used to measure the Hall coefficient. To determine the Hall coefficient, the current was applied along one diagonal of the sample, while the Hall voltage was measured perpendicular to it. The Hall voltage was measured along both diagonals of the near square shaped sample and at positive and negative magnetic fields to account for geometric effects in the pin placement and sample geometry. In each magnetic field and current orientation, the current direction was alternated in a delta-measurement to account for electromotive forces [28], thermally induced through minuscule temperature gradients inside the sample. A HP 3488A Switch/Control unit was used to automatically change pin connections for resistivity and the Hall coefficient measurements. The error bars for the resistivity measurements represent a statistical standard deviation of 20 repeated measurements, while the error bars for the Hall coefficient depict the propagated error of the statistical standard deviation of 6 successive voltage measurements in each geometry and field.

Scanning transmission electron microscopy (STEM) measurements were performed to combine reciprocal and real space information from the same spatial location of the sample at high resolution. Selected samples were examined in cross-section geometry using Titan Themis 200 from FEI operated at 200,000 V. The cross-section lamellae of W/CoFe bilayered films were prepared perpendicular to the side of the samples using a focused ion beam (FIB) Zeiss FIB/SEM Crossbeam 550 with Ga Ion-Sculptor gun system. The final polishing was performed at 5000 V ion acceleration voltage with XeF$_2$ gas assistance.

2.3 Density functional theory calculations

Density functional theory (DFT) [29] was employed at 0 K to explore the atomic and electronic structure of two interfaces, namely W (110) on Al$_2$O$_3$ (11$\bar{2}$0) with W [1$\bar{1}$1]‖Al$_2$O$_3$ [0001] as well as W (001) on MgO (001) with W [100]‖MgO [110]. The Vienna *ab initio* simulation package was used. The projector augmented wave potentials were chosen for the basis set [30–32] and the generalized gradient approximation, as parameterized by Perdew, Burke, and Ernzerhof [33], was used to describe the exchange-correlation effects. The Blöchl correction was employed [34] for the interfaces and an integration over the Brillouin zone was performed with the Monkhorst-Pack approach [35] with a k-point mesh of 4×4×1 for W (110) on Al$_2$O$_3$ (11$\bar{2}$0) (198 atoms) and 8×8×1 for W (001) on MgO (001) (112 atoms). The convergence tests regarding the slab (substrate) thickness and k-points were carried out previously [36]. Default values for the energy cut-off were taken into account.

Considering the size of the Al_2O_3/W configuration (198 atoms), larger lateral configurations were not probed due to limited computational resources, but similar slab thicknesses, i.e., the number of stacked layers, for both interfaces were considered so that the results should be comparable. Six layers of W were always stacked on each substrate. The orthorhombic description of corundum Al_2O_3 was used to construct the interfaces [36]. Oxygen termination of the Al_2O_3 ($11\bar{2}0$) surface was assumed as it is reported to be a more likely match of the actual substrate surface in the experiments [37–40]. Our intention was to compare equivalent bonds across the interfaces (W–O for both W/Al_2O_3 and W/MgO rather than W–Al for W/Al_2O_3 and W–O for W/MgO). Hence, the calculated values of work of separation indicate likely trends to occur experimentally. 6 atomic layers of W were taken into account, whereby W atoms were placed at the top position of O atoms. The convergence criterion for the total energy was 0.01 meV and the cut-off energy was 500 eV. All interfaces were constrained to the calculated lattice parameters of bulk Al_2O_3 and MgO at 0 K, acting as substrates. To construct these interfaces, a vacuum layer was inserted perpendicularly to the interface with a thickness of 10 Å. The bottom layer of each substrate was frozen to mimic the infinite bulk. The interfaces were characterized by a work of separation W_S [36, 41], calculated from the total energy change per unit area upon separation of the corresponding slabs. All counterparts were fully relaxed at 0 K. The electronic structure was characterized by evaluating electron density distributions.

3 Results and discussion

3.1 Growth of epitaxial W thin films

To compare the epitaxial growth of single layers of W on Al_2O_3 ($11\bar{2}0$) and MgO (001) substrates, thin films, 100 Å in thickness, were sputtered under the same deposition conditions. Their x-ray scattering patterns are displayed in the upper panel of Fig. 1. We start the discussion on the structural quality by having a closer look on the layering of the films, i.e., the low angle scattering regime displayed in detail in Fig. 1a. Both patterns show pronounced Kiessig fringes [42] up until 10° and 12° in 2θ for the films grown on Al_2O_3 ($11\bar{2}0$) and MgO (001), respectively. The presence of Kiessig fringes up to 10° is typically only found in layers

Fig. 1 X-ray scattering patterns of 100 Å W layers grown on single crystalline Al_2O_3 ($11\bar{2}0$) and MgO (001) substrates. The films are capped with 30 Å Al. Indexed peaks relate to the α-W structure. The highlighted regions in the upper panel are displayed as (**a–d**) in the panels below. Red curves correspond to fits of **a** the reflectivity and **b–d** the indicated Bragg peaks indexed hkl. From the fits, **a** the scattering length density SLD profiles over thickness z and **c** the evolution of out-of-plane lattice spacing d_{hkl} over n lattice planes were obtained and are shown as insets. The grey dashed line corresponds to the d_{hkl} spacing of the equilibrium α-W structure [16, 17]. For (**b**, **d**) no strain profile was applied. The scattering patterns are shifted vertically for clarity
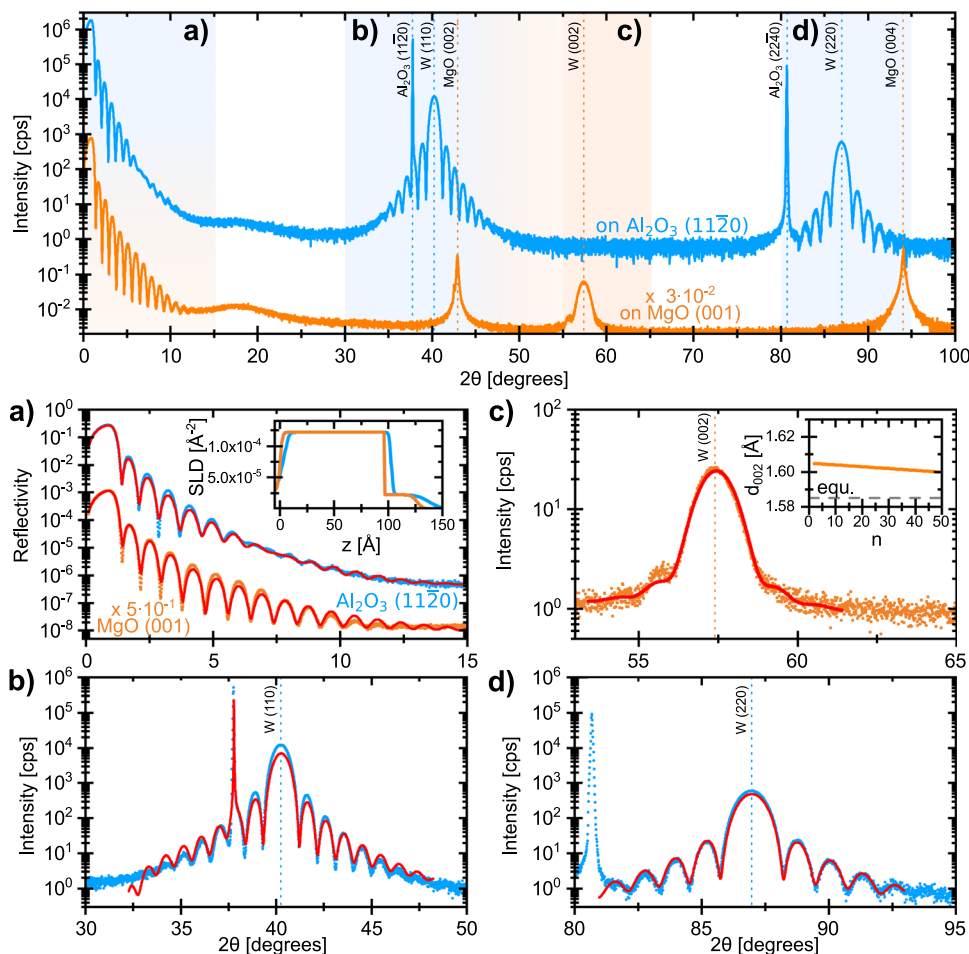
that are flat on a mesoscopic length scale of the order of the in-plane coherence length of the x-ray beam. Scattering length density profiles obtained from the fitting of the reflectivity are shown as insets and confirm the intended substrate/W/Al layering with well defined layer thicknesses on both substrates.

For the thin film grown on Al_2O_3 (11$\bar{2}$0), the interface widths and surface roughness of the substrate, the 97(1) Å W layer, and the 35(1) Å Al layer are 2(1), 2(1) and 9(1) Å, respectively. The interface widths and surface roughness of the MgO (001) substrate, the 97(1) Å W layer, and the 30(1) Å Al layer are 2(1), 0(1), and 4(1) Å, respectively. Furthermore, for Al_2O_3 (11$\bar{2}$0), the reflectivity data could only be fitted by including an additional 5(1) Å layer with a roughness of 3(1) Å at the substrate/W interface in the fit, with electronic density close to tungsten oxide. Since roughness and thickness of this layer are of the same order of magnitude, the roughness value may not be indicative of the real underlying roughness. A similar observation has been made for Nb growing on sapphire, relating the presence of an oxide layer to a kinematic chemical reaction between a film and a substrate [20]. The observation is in line with the reported bonds forming between W atoms growing on Al_2O_3 and the oxygen atoms of the substrate [43]. As the nominal thicknesses for all samples lie reasonably close (< 4% for W and CoFe) to the fitted layer thicknesses, we will continue to refer to the nominal thickness henceforth.

Regarding the diffraction analysis of the W thin film grown on Al_2O_3 (11$\bar{2}$0), two peaks corresponding to the (110) and (220) α-W structure Bragg reflections are visible at 40.254(0) and 86.962(1)°, corresponding to the out-of-plane atomic distances d_{110} and d_{220} in W of 2.239(0) and 1.119(0) Å, respectively. Since the Bragg peaks of the β–W structure lie within a few degrees of the observed (110) and (220) peaks [44–46], reciprocal space mapping was conducted around the α–W (002) reflection at 58° [16, 17, 47] in 2θ. At a tilt χ of the sample by 45° perpendicular to the scattering plane, we observed a sharp peak, confirming the phase-pure epitaxial growth of α-W on Al_2O_3 (11$\bar{2}$0) with [110] out-of-plane growth direction under the above mentioned conditions. For simplicity, α-W is referred to as W for growth on Al_2O_3 (11$\bar{2}$0) henceforth. The sharp peaks, namely Al_2O_3 (11$\bar{2}$0) and (22$\bar{4}$0), are attributed to the substrate, while the broad bump at around 18° is attributed to the amorphous capping layer.

In addition, around the W (110) and (220) Bragg peaks, magnified in Fig. 1b, d, respectively, symmetric Laue oscillations are visible over a range of more than 10°. The occurrence of the Laue oscillations is proof of a high degree of coherent scattering and, therefore, high crystal quality over the total thickness of the W layer [20, 48]. As defects and dislocations give rise to coherent diffuse scattering and do not contribute to the observed intensity of these oscillations,

the shape and decay of the Laue oscillations can be used as a quantitative measure for the crystal quality of epitaxial thin films [48]. The diffracted intensity around the W (110) and (220) Bragg peaks was fitted to identify the degree of coherent scattering. Fits are shown as red lines in the respective figures. The symmetry of the oscillations indicates a negligible degree of strain in the 100 Å thick W layer [49], which is in line with the reports on epitaxial W growth on sapphire by pulsed laser deposition [50]. Hence, no strain profile was included in the fitting for the sample grown on Al_2O_3 (11$\bar{2}$0).

As it is evident from Fig. 1, the fitting captures the features of the diffraction pattern. The main (110) Bragg peak intensity however is not entirely captured, with the fitted interface roughness being underestimated. Based on both fits, 99.9% of the pure W layer scatters coherently. It has to be noted, however, that the thickness of the tungsten oxide resembling interface layer in the XRR fitting was not included in this calculation due to its unknown crystal structure. Including it by assuming the obtained average W layer spacing of the film above, yields a reduced percentage of 94.7%. The fitted average out-of-plane distances d_{110} and d_{220} lie within 0.1% of the previously determined values. The interface roughnesses, contributing to the decay of the intensity of the Laue oscillations with increasing angular distance from the W (110) and (220) main peaks, are fitted to be 2 and 5 Å, respectively, and thus in agreement with the fitted roughnesses based on the reflectivity data.

On MgO (001), the only observed specular W peak is at 57.404(2)° and corresponds to a d_{002} of 1.604(0) Å of the α-W structure. For simplicity, α-W is henceforth also referred to as W for growth on MgO (001). The sharp MgO (002) and (004) peaks are attributed to the single crystalline substrate. W is growing epitaxially in the [001] growth direction on MgO (001), in line with results from previous studies [51]. However, in this study, Laue oscillations are observed on the low angle side, observable in the magnified display of the W (002) Bragg peak in Fig. 1c. The oscillations are less pronounced, decay faster, and are more asymmetric compared to W grown on Al_2O_3 (11$\bar{2}$0). In the fitting, the asymmetry is accounted for by a strain profile. The fitted variation of the out-of-plane spacing d_{002} as a function of lattice planes n across the W layer thickness is shown in the inset. The out-of-plane spacing seems to be linearly decreasing over W layer thickness, lying around 2% above the equilibrium lattice spacing of bulk W [16, 17]. Lattice mismatch between film and substrate gives rise to misfit strain in epitaxial thin films causing a change in out-of-plane lattice spacing over film thickness. The origin of strain in W grown on MgO (001) will be discussed below. Based on the fitting, 80.4% of the W layer grown on MgO (001) scatter coherently. The fitted d_{002} lies within 0.1% from the previously determined value, and the

interface roughness of 5 Å is in agreement with the roughness obtained from XRR.

The degree of coherent scattering of the W layer can, as discussed above, be used as a quantitative measure of the crystal quality of epitaxial W, which is higher for Al_2O_3 ($11\bar{2}0$) than that for MgO (001). Moreover, the observed difference in the crystal quality manifests itself in the peak intensity distribution in reciprocal space. The peak intensity of the Bragg peaks is one to three orders of magnitude higher for W on Al_2O_3 ($11\bar{2}0$) compared to W on MgO (001). This difference is related to a larger mosaic spread of W grown on MgO (001), as it can be seen in the upper panel of Fig. 2. The rocking curve around the W (110) peak for W grown on Al_2O_3 ($11\bar{2}0$) is sharp and has a full width at half maximum (FWHM) of 0.02(0)°. The peak intensity of the rocking curve around the W (002) peak for W grown MgO (001) is distributed over a two orders of magnitude wider angular range (FWHM = 2.19(5)°). The instrument

resolution of 0.012° was taken into account for determining these values. The mosaic spread, i.e. misorientation of the W atomic planes relative to each other, is larger, corresponding to a lower crystal quality of the film grown on MgO (001).

As the mosaic spread of the epitaxial W thin film on Al_2O_3 ($11\bar{2}0$) is low, it is possible to grow relatively thick films still exhibiting a high degree of coherent scattering. The diffractogram around the W (110) Bragg peak of a 1000 Å thick W layer is shown in the lower panel of Fig. 2. Even for this tenfold larger layer thickness, W grows epitaxially with [110] growth direction on Al_2O_3 ($11\bar{2}0$). The Bragg peak position relates to an average d_{110} spacing over 1000 Å of 2.240(0) Å, a deviation of less than 0.08 % from d_{110} for 100 Å W. The Laue oscillations observed on both sides are symmetric and can be observed over a range of more than 4° in 2θ, being proof of a small degree of strain over the W layer thickness. To the best of the authors' knowledge, the Laue oscillations of W have only been observed for thin films of 30 Å layer thickness [50]. The existence of the Laue oscillations for a film thickness of 1000 Å is proof of the superior crystal quality of the W films deposited in this study. It showcases that the crystal quality is not deteriorating with thickness and up until 1000 Å thickness there is no onset of relaxation through dislocations in the film. The FWHM of 0.04(0)° of the (110) rocking curve for 1000 Å W, shown in the inset, is comparable to the value for 100 Å W. However, the shape of the rocking curve for 1000 Å W includes two features indicating two different correlation lengths; a narrow feature, almost resolution limited, and a broader triangularly shaped feature. Similar observations of features in rocking curves have been reported for epitaxial Nb (110) grown on Al_2O_3 ($11\bar{2}0$) [20], where the broad feature is more pronounced for thicker films. For Nb, Wildes et al. [20] show that flat growth planes over long length scales give rise to the narrow component, while strain and misfit dislocations causing height deviations give rise to the broader feature in the rocking curve. The integrated intensity of the broad component is thickness dependent for Nb, which is attributed to an increased layer roughness for thicker films [52]. The broad component can be viewed as related to the defect density. For Nb, a large part of the relaxation takes place at the substrate/Nb interface, i.e. it is semicoherent. Due to the similarity between the observed scattering from Nb(110) and W(110) thin films grown on Al_2O_3 ($11\bar{2}0$), relaxation at a semicoherent substrate interface is likely to also be present in W thin films.

Hetero-epitaxy is restricted to specific relative orientations of substrate and film, as lattice matching is required. On Al_2O_3 ($11\bar{2}0$), epitaxial W (110) growth is observed due to a match between these two crystal planes at the substrate interface. The W (110) crystal plane has a rectangular atomic shape with the atomic distance d_{110} on one side and d_{001} on
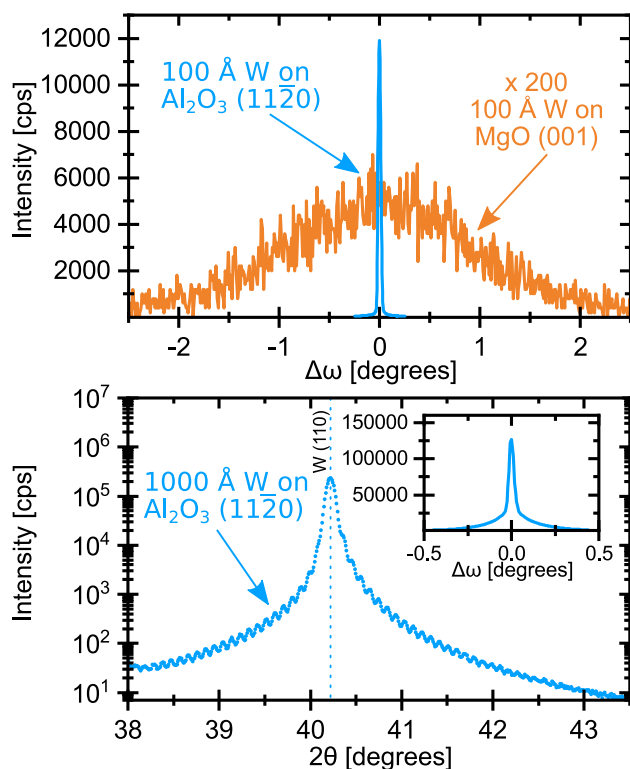

Fig. 2 Top panel: Rocking curves measurements around the specular α-W Bragg peak of 100 Å W grown on single crystalline Al_2O_3 ($11\bar{2}0$) and MgO (001) substrates. For Al_2O_3 the measurement was conducted around the W (110) Bragg peak and for MgO the measurement was conducted around the W (002) Bragg peak. To visually compare the widths, the rocking curve of the sample grown on MgO was multiplied by a factor of 200. Bottom panel: X-ray diffraction pattern around the W (110) Bragg peak of 1000 Å W grown on single crystalline Al_2O_3 ($11\bar{2}0$). The rocking curve for this peak is displayed in the inset

the other side. The Al_2O_3 [0001] and [1$\bar{1}$00] directions span the corresponding Al_2O_3 (11$\bar{2}$0) plane [50, 53]. It is reported that a W (110) growth orientation with an in-plane rotated unit cell is energetically favored to match a rectangular structure on the Al_2O_3 (11$\bar{2}$0) surface [20, 50, 53, 54].

Based on the work of Mc Grath et al. [50], this rotation is calculated to be 54.7° relative to Al_2O_3 [0001] or 35.3° relative to [1$\bar{1}$00]. To further investigate the in-plane orientation of the W unit cell in our thin films, a W {112} pole figure measurement was conducted on a 1000 Å thick W layer. The results are displayed in Fig. 3. The off-specular W {112} peaks are expected to be observed in diffraction at the incident angle θ corresponding to d_{112}. However, to obtain a W {112} plane in diffraction, the sample needs to be tilted by a certain polar angle χ and rotated by the azimuthal angle ϕ based on the in-plane orientation of the unit cell relative to (110) out-of-plane orientation. The pole figure displays the polar angle χ (sample tilt) and the azimuthal angle ϕ (sample rotation). At $\phi = 0°$, the sample edges, corresponding to the Al_2O_3 [0001] and [1$\bar{1}$00] directions, are oriented 90° and 180° to the incoming x-ray beam. Sharp peaks are observed at specific χ and ϕ angles, confirming epitaxial growth of 1000 Å W on Al_2O_3 (11$\bar{2}$0).
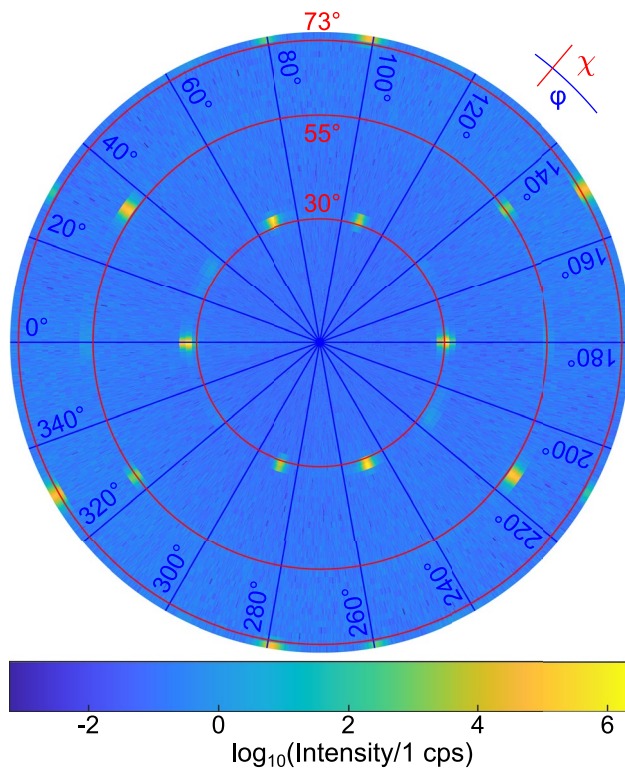
Fig. 3 W {112} x-ray pole figure measured on a 1000 Å W layer grown on single crystalline Al_2O_3 (11$\bar{2}$0). The pole figure displays the polar angle χ (sample tilt) and the azimuthal angle ϕ (sample rotation). Specific χ and ϕ values relevant for the discussion are marked as red circles and blue lines, respectively

The angles between [110] and <112> are all either 30.0°, 54.7°, 73.2°, or 90.0°, depending on the specific crystallographic plane from the <112> family. These χ angles are displayed as red circles. Within the resolution of the measurements related to the angles χ and ϕ, the {112} peaks are observed at these specific sample tilts, in line with the expected small degree of strain in the epitaxial W film. Moreover, a {112} peak is observed at $\phi = 0°$ and 180° for $\chi = 30.0°$. Therefore, a W <112> crystallographic direction is assumed to be parallel to the edge of the substrate, which is either [0001] or [1$\bar{1}$00] spanning the Al_2O_3 (11$\bar{2}$0) plane.

To determine the relative crystal orientation of the substrate and the film, an Al_2O_3 {11$\bar{2}$0} pole figure was measured for $\phi = -10°$ to 110° and $\chi = 0°$ to 80°. The only visible {11$\bar{2}$0} peak measured within this range is at $\phi = 0°$ and for a sample tilt of $\chi = 60°$. In a hexagonal crystal with (2$\bar{1}$$\bar{1}$0) orientation, (11$\bar{2}$0) satisfies the diffraction criterion for a 60° sample tilt χ with [0001] rotation axis. Therefore, at $\phi = 0°$, [0001] is parallel to a W {112} plane and thus perpendicular to the respective <112> direction. Hence, our experimental diffraction study confirms the epitaxial relationships reported by Mc Grath et al. [50]: W[1$\bar{1}$1]||Al_2O_3[0001] and W[$\bar{1}$12]||Al_2O_3[1$\bar{1}$00] or W[1$\bar{1}$$\bar{1}$]||$Al_2O_3$[0001] and W[1$\bar{1}$2]|| Al_2O_3[1$\bar{1}$00].

The lattice mismatch for these epitaxial relationships are 7.2 % and 19.4 % along the W [1$\bar{1}$1] and W [$\bar{1}$12] directions, respectively [16, 17, 55]. The mismatch is expected to cause misfit strain in the growing W layer, eventually leading to the formation of misfit dislocations and strain release above the critical thickness for fully coherent growth. Due to the positive Poisson ratio of 0.284, determined from reported elastic constants [56], the strain in W is expected to be tensile in-plane and compressive out-of-plane since both atomic distances in Al_2O_3 are larger compared to the corresponding atomic distances in bulk W. For comparison, for the epitaxial growth of similar sized Nb (110) on Al_2O_3 (11$\bar{2}$0), lattice mismatches of 1.9% and 12.9% are reported in the two different crystallographic directions [54] and the critical thickness is reported to be less than 100 Å [20]. Hence, for the W films grown within this study, we expect the formation of misfit dislocations for strain release giving rise to coherent diffuse scattering, which reduces the coherence length of the epitaxial crystal [57]. However, parts of this dislocation formation is expected directly at the substrate/film interface for two reasons: First, in the stated epitaxial relationship, some W atomic positions do not coincide with atomic positions of the Al_2O_3 lattice, but lie close to octahedral interstices in the Al_2O_3 lattice [20, 50]. Therefore, additional atomic relaxation is expected at the interface. Second, a miscut is common for the Al_2O_3 (11$\bar{2}$0) substrates [20, 24] that causes atomic steps and terraces with an incommensurate step height of d_{0006}. Therefore, the terraces will propagate into the growing

film as defects. In between the defects, coherent regions with well-defined translational order are expected [20]. The presence of defects at the substrate/film interface is supported by the necessity to include an additional layer into the XRR fitting for both W and Nb [20] grown with (110) texture on Al_2O_3 ($11\bar{2}0$). The defects are expected to reduce the misfit strain in W already at the interface, below the critical thickness. For Nb (110) on Al_2O_3, residual epitaxial strain which depends on the layer thickness is reported to lie usually below 0.05% [19]. Hence, growth with reduced misfit strain above the interface is expected for W on Al_2O_3 ($11\bar{2}0$), in line with the result that 99.9 % of the relaxed W layer on top scatter coherently.

The conundrum of obtaining epitaxy despite a large misfit strain requires further investigation. For that reason, DFT calculations of the epitaxial Al_2O_3 ($11\bar{2}0$)/W (110) interface structure were performed. The results on the crystal structure including the corresponding electron density distribution are displayed in Fig. 4a. Based on these, strain is introduced into the growing W layer at the interface, as evident from the tetragonal distortion of the W slab. To match the in-plane atomic distances in the substrate, the in-plane atomic spacing $d_{1\bar{1}0}$ at the interface was calculated to be 2.774 Å, an increase of 23% compared to 2.242 Å [16, 17] at equilibrium, which is in line with the expected in-plane tensile strain. In the out-of-plane direction, the calculations predict a significantly larger $d_{110} = 2.671$ Å between the first and second atomic layers compared to the interplanar spacing of the following monolayers. Furthermore, the DFT calculations indicate that the first atomic layer of W exhibits a buckled atomic structure. The center atom in the (110) atomic plane has a larger distance to the interface as compared to the oxygen bound corner atoms in the unit cell. Such buckling often occurs due to high interfacial strains [58]. The exceptionally large interplanar spacing between the first and second atomic W layer in combination with the buckling of the atomic structure can be assigned to different chemical and structural properties of W directly at the interface, in agreement with the tungsten oxide resembling interface layer included in the XRR fitting as well as the expected strain relaxation at the interface. From the electron density distribution of the interface structure, a change in electron density of the first three monolayers is evident, showing an out-of-plane elongation of the area of high electron density around the atomic positions. First-principles calculations on the similar Al_2O_3 (0001)/Nb (111) system also show appreciable interlayer relaxation near the interface for an oxygen terminated substrate surface [59]. However, all calculated atomic distances in W are larger than the equilibrium d_{011} of 2.242 Å [16, 17]. This out-of-plane elongation is in contrast to the expected compressive strain in this direction and to the experimentally observed smaller d_{011} in the out-of-plane direction of around 2.239(0) and 2.240(0) Å for the 100 and
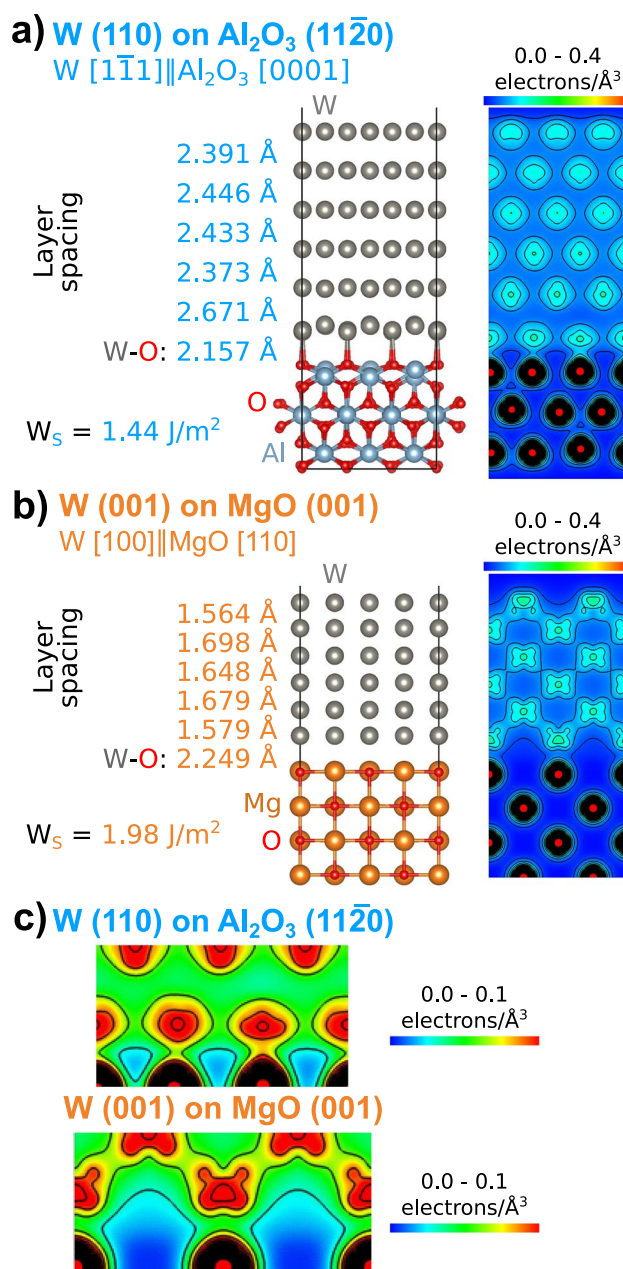

Fig. 4 Results of density functional theory calculations of 6 monolayers of **a** W (110) on Al_2O_3 ($11\bar{2}0$) with W [$1\bar{1}1$]‖Al_2O_3 [0001] and **b** W (001) on MgO (001) with W [100]‖MgO [110]. A schematic of the atomic structure and the electron density distributions of the interface are displayed in the middle and to the right of each figure, respectively. In-plane and out-of-plane atomic distances at the interfaces and in the W layers are indicated. The work of separation W_S is displayed on the left side. For Al_2O_3, oxygen surface termination is assumed. **c** Zoom-in of the electron density maps onto the substrate/W interface

1000 Å thick W layers, respectively. It should be remarked that the high interfacial strains and hence high atomic relaxations are partly due to the interface size. Classical molecular

dynamics modelling may reveal these particularities, but we are not aware of any available interatomic potentials.

The calculated work of separation W_S for the Al_2O_3/W (110) system with W $[1\bar{1}1]\|Al_2O_3[0001]$ is 1.44 J/m^2, corresponding to an intermediately strong interface where epitaxy may be possible. For substrate/film combinations known for their epitaxial growth like Nb(111) on Al_2O_3 (0001) or Cu(111) on Al_2O_3(0001) larger values for W_S are reported, namely 12.7 [60] and 5.48 J/m^2 [61], respectively. A comparable work of separation of 2.86 J/m^2 is reported for V_2AlC(0001) on Al_2O_3 (11$\bar{2}$0) [36]. The interface of Al_2O_3 (11$\bar{2}$0)/V_2AlC(0001) was characterized as semicoherent, i.e. having coherent regions separated by misfit dislocations due to a lattice mismatch of 8.16% [36].

Results of temperature dependent electronic resistivity measurements of 1000 Å W grown on Al_2O_3 (11$\bar{2}$0) are displayed in Fig. 5. The statistical error of each data point is of the order of 1×10^{-4} $\mu\Omega$cm and thus smaller than the symbols depicted. The data exhibits a typical Bloch-Grüneisen metallic behaviour with a residual resistivity ratio (RRR) of 3.14. The ratio is comparable to the value reported by Choi et al. [62], with a RRR of around 4 for annealed samples. Hence we conclude that the defect density in the present samples are comparable to the state of the art of epitaxial tungsten films grown with sputtering. While the previous discussion of the XRD data strongly suggests excellent crystal quality, the measured RRR in this case remains relatively low. One possible explanation for this disparity could lie in the origin of the XRD and resistivity signals. The XRD intensities arise from coherent scattering within the coherence volume of the x-ray beam, typically limited to a few thousands Ångströms. Conversely, the resistivity signal probes the entire sample area, with the probing pins separated by several millimeters.

The Hall coefficient in the present sample is about half of the bulk value of 11.3$\times 10^{-11}$ m^3/C [63] at 300 K and decreases with decreasing temperature. In contrast to the bulk sample of [63], it exhibits a crossover close to 85 K.
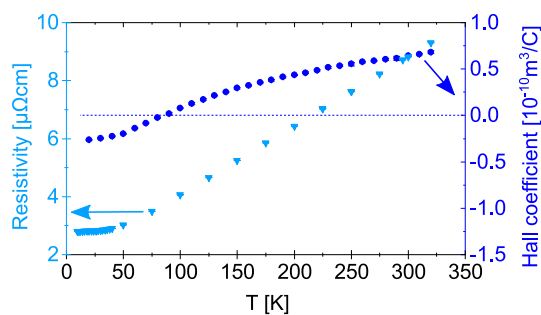

Fig. 5 Temperature dependent electronic resistivity and Hall coefficient measurements of a 1000 Å thick W layer grown on Al_2O_3 (11$\bar{2}$0)

Care is needed when comparing results of measurements on single crystals to polycrystalline materials, since the Hall effect depends on the crystallographic direction [63–65]. An increase in the crystallographic defect density is expected to increase the resistivity and alter the Hall coefficient. However, the influence of defects on the Hall coefficient are due to their impact on the anisotropy of the scattering rates rather than their absolute value [66]. Furthermore, the Fuchs-Sondheimer model of surface scattering predicts an increase of resistivity and the Hall coefficient with decreasing film thickness [62, 67] with the present film being reasonably close to the bulk regime, where finite size is not seriously affecting the results. The behaviour of the Hall coefficient versus temperature in Fig. 5 exhibits the opposite trend as that of α-W films grown on thermally oxidized Si, as reported by Hao et al. [10], whereas β-W, exhibits consistently negative Hall coefficients at temperatures between 10 and 300 K [10]. This interesting difference in the sign and the magnitude of the Hall effect as compared to [10] might be due to the large difference in defect densities, phase purity, and/or crystallographic orientation, between the epitaxially grown films here and the textured films grown by Hao et al. [10]. In fact, Bastl [68] concluded from Hall measurements on thin polycrystalline films of W that the presence of grain boundaries together with defects resulted in a suppression of the Hall coefficient as compared to the bulk value. The sign of the Hall coefficient in the present work was confirmed (at ambient temperature) by comparing the results of measurements of the Hall coefficient in the same setup of other polycrystalline bulk samples to the literature.

In contrast to the epitaxial W thin film grown on Al_2O_3 (11$\bar{2}$0), W grown on MgO (001) exhibits the [001] out-of-plane growth direction. Epitaxial growth of W on MgO (001) was confirmed as off-specular peaks were measured as sharp reflections occurring at specific sample tilts χ and rotations ϕ in reciprocal space. Measurements of the off-specular W {112} reflections revealed a relative in-plane rotation of 45° between the W [100] and MgO [100] directions, i.e. W [100] is oriented parallel to MgO [110], confirming the epitaxial relationship reported elsewhere [51]. This in-plane rotation allows for a smaller mismatch of around −6.1 % between the respective atomic distances in film and substrate [16, 17, 51]. At elevated deposition temperatures like 843 K, the lattice mismatch is expected to be even smaller due to different thermal expansion coefficients of substrate and film [51]. Such a lattice rotation has been reported for other epitaxially growing thin films on MgO (001) substrates with similar atomic distances as W, e.g. Fe [69–71], V, Cr, Hf [25] or alloys thereof [72]. The mismatch is negative [20], yielding compressive in-plane and tensile out-of-plane strain in W and hence, a tetragonally distorted unit cell. It is the opposite strain state as compared to W grown on Al_2O_3 (11$\bar{2}$0). Hints of the expected tetragonal distortion of the

unit cell can be found in the asymmetry of the Laue oscillations for W grown on MgO (001), displayed in Fig. 1c. The critical thickness for the introduction of misfit dislocations of W grown at 1173 K on MgO (001) with a mismatch of − 5.1 % is reported to be 27 Å, well below the W thicknesses in this study. Hence, misfit dislocation formation is expected for all samples of W grown on MgO (001). The variation of the out-of-plane atomic distance d_{200} over the thickness of the W layer lies above the equilibrium spacing for relaxed W [16, 17], in line with tensile out-of-plane strain. Over the layer thickness, d_{002} is decreasing towards the equilibrium value, indicating a partial strain relaxation.

These observations are in agreement with DFT calculations on the crystal structure of the MgO (001)/W (001) interface. The results of these calculations are displayed in Fig. 4b. The in-plane d_{100} lattice distance is calculated to be 3.004 Å and, thus, smaller than the equilibrium value [15–17], but in line with the expected compressive in-plane strain. It appears that W is tetragonally distorted for the first six monolayers, whereby the out-of-plane interplanar spacing is larger than that of the equilibrium configuration, as expected for the tensile strain state in this direction. The spacing oscillates between roughly 1.60 and 1.69 Å for every other layer. This highlights that the expected strain might affect atoms at different positions of the bcc cell differently, possibly due to different in-plane positions in relation to the substrate. Another reason may be the employed registry, since lateral relaxations may partly be inhibited due to the size of interface considered by DFT.

The calculated work of separation W_S is similar to the value calculated for W (110) on Al_2O_3 (11$\bar{2}$0). The interface is thereby characterized to be intermediately strong, allowing for epitaxy, possibly locally or up to low W thicknesses. The interfacial bonds between tungsten and the oxygen atoms of the substrate, however, are weaker in the case of MgO (001). This difference is also visible in the electron density map. In the case of both interfaces, the interfacial bonds are characterized by covalent contributions (charge sharing) and ionic contributions (charge transfer). Figure 4c contains a zoom-in of the electron density distribution at the substrate/W interfaces. Up to 30 % more charge is shared between W and O across the W/Al_2O_3 interface compared to W and O across the W/MgO interface implying a stronger covalent interaction. The bonds between W and O atoms across the Al_2O_3/W interface are shorter and thus stronger than those in the case of MgO, but a more transparent comparison should be made by comparing the bond lengths in the substrates (bulk counterparts). The Mg-O bond length is 2.124 Å, while the corresponding interfacial bond (W–O) is 2.249 Å. On the other hand, the Al–O bond length in the substrate is 1.874 Å and the corresponding W–O bond is 2.157 Å. Hence, a stacking sequence together with an expected bond length is better

reproduced for W on MgO (001), which is mirrored in the slightly higher work of separation.

We established that the epitaxial growth and quality of W thin films are highly dependent on substrate and thin film thickness. Following this, the dependence on the deposition temperature will now be discussed. Figure 6 shows a diffraction pattern around the W (220) Bragg peak of two 100 Å thick W thin films grown at different deposition temperatures on Al_2O_3 (11$\bar{2}$0) substrates. With an increase in deposition temperature of 50 K, the Bragg peak position shifts slightly towards higher 2θ angles, corresponding to an atomic spacing d_{220} of 1.119(0) Å and 1.118(0) Å for 793(2) and 843(2) K, respectively. A more distinct difference is visible in the Laue oscillations around the main peak, which are visible over an angular range of 8° and 10° for 843(2) and 793(2) K, respectively.

While the Laue oscillations are symmetric for the sample grown at 793(2) K, they show an asymmetry for the sample deposited at 843(2) K, decaying faster on the low than on the high angle side. In contrast, epitaxial W grown on MgO (001) or Fe on $MgAl_2O_4$ (001) [49] exhibit Laue oscillations around the main Bragg peaks which decay faster on the high than on the low angle side. This difference in decay is attributed to the opposite strain state and therefore, tensile instead of compressive out-of-plane strain. Hence, for W grown on Al_2O_3 (11$\bar{2}$0), the out-of-plane lattice spacing is expected to increase over the layer thickness due to strain relaxation. The change in symmetry with growth temperature observed in Fig. 6 shows that the introduction of misfit dislocations for strain relaxation in W thin films is thermal energy dependent. The increase in deposition temperature by 50 K might lead to an increase in ad-atom mobility at the interface, partly preventing relaxation through the introduction of misfit dislocations. For the film grown at 843(2) K misfit dislocations are possibly incorporated into the growing W layer at slightly larger layer thicknesses while relaxation is expected to take place at the substrate/W interface for
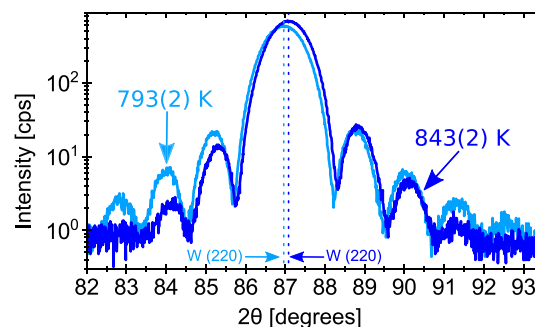

Fig. 6 X-ray diffraction patterns of 100 Å W layers grown at 793(2) and 843(2) K on single crystalline Al_2O_3 (11$\bar{2}$0) substrates. The films are capped with 30 Å Al. The indexed peak relates to the α-W structure

W grown at 793(2) K. This is in line with the smaller inter-planar spacing of the sample deposited at 843(2) K, since it corresponds to an average over the W layer thickness. The degree of the observed asymmetry in this sample is, how-ever, smaller than expected from the large lattice mismatch for Al_2O_3 ($11\bar{2}0$)/W (110), indicating that a large part of the strain is still released at the substrate/W interface. For W on Al_2O_3 ($11\bar{2}0$) grown at 843(2) K, the relative range of the oscillations on the faster decaying side is roughly 38 % of the whole range of oscillations. For W (001) grown on MgO (001) with a smaller lattice mismatch of −6.5 % and Fe (001) on $MgAl_2O_4$ (001) with a lattice mismatch of only −0.2 % the relative range spans 29% and 15% [49], respectively. As W shows this intriguing growth temperature dependence in its crystal quality, the exact kinetic implica-tions on the formation of dislocations at different thicknesses in the growing W layers will be part of an upcoming study.

3.2 Growth of tungsten and CoFe bilayers

Building on the knowledge about epitaxial W single layer growth, W/CoFe bilayers of different layer thicknesses have been deposited. X-ray scattering patterns of a "thick" 60 Å W/100 Å CoFe and a "thin" 30 Å W/25 Å CoFe bilayer sample both grown on Al_2O_3 ($11\bar{2}0$) are displayed in Fig. 7. In the small angle regime, Kiessig fringes [42] are visible. As their spacing relates to the total film thickness including all layers, broader fringes are observed for the "thin" bilayer sample. The fringes decay at around 10° and 8° in 2θ for the "thick" and "thin" bilayer sample, respectively.

In diffraction, sharp peaks corresponding to the Al_2O_3 ($11\bar{2}0$) and ($22\bar{4}0$) reflections of the substrate are vis-ible for both samples. Two peaks can be attributed to epi-taxially growing W with (110) out-of-plane orientation, namely W (110) and (220), in line with the observations for W single layers on Al_2O_3 ($11\bar{2}0$) substrates. The width of the Bragg peaks is larger as compared to the ones of the W single layers in Fig. 1, since the W thickness is reduced [73]. Based on scans around off-specular reflections, the

sole presence of the α-W structure is confirmed even for the thinnest W layer in this study with a thickness of 30 Å. The W peak positions relate to atomic spacings d_{110} and d_{220} of 2.235(0) and 1.118(0) Å for the "thick" sample and 2.221(0) and 1.118(0) Å for the "thin" bilayer sample. The change in d_{110} and d_{220} with W layer thickness between 30 and 1000 Å is below 0.9 %, in agreement with the described strain relaxation at the substrate/W interface and not over the W layer thickness.

For the "thick" sample, peaks corresponding to the CoFe (110) and (220) Bragg reflections [16, 74] are observed at 44.981(5)° and 99.940(7)° in 2θ. As no other peaks in the specular $2\theta - \theta$ scan can be attributed to CoFe, the layer is assumed to at least grow highly textured, in line with the observed FWHM of the CoFe (220) rocking curve of 0.06(0)°. The corresponding d_{110} and d_{220} are 2.014(0) and 1.006(0) Å, respectively. The equilibrium interplanar spacings d_{001} and $d_{1\bar{1}0}$ in CoFe have a mismatch to the cor-responding distances in W of approximately 12 % each [16, 17, 74]. Based on its positive Poisson's ratio of 0.397 [75], CoFe (110) is assumed to grow with tensile in-plane and compressive out-of-plane strain on W (110). Moreover, indications of fully epitaxial growth of parts of the CoFe layer are present in the form of Laue oscillations of two different average oscillation frequencies of approximately $f_1 = 1.5$ degrees^{-1} and $f_2 = 0.6$ degrees^{-1}, between 35° and 48° in 2θ.

This oscillation frequency is directly related to the coher-ently scattering thickness: the oscillations of the lower fre-quency f_1 can be related to a thickness of 59 Å, which is in the order of 98 % of the W layer thickness, while the higher frequency f_2 oscillations relate to a thickness of around 147 Å, which is in the order of 92 % of the bilayer thick-ness. The observation of Laue oscillations relating to the bilayer thickness are proof of coherent scattering through-out both layers [76]. In contrast, no Laue oscillations with a frequency relating to the CoFe single layer thickness are observed around the CoFe (110) or (220) Bragg peaks. This can be attributed to multiple possible reasons: First,

Fig. 7 X-ray scattering patterns of W/CoFe bilayers grown on single crystalline Al_2O_3 ($11\bar{2}0$) substrates. Indexed peaks relate to the α-W structure. The film corresponding to the upper pattern consists of 60 Å W and 100 Å CoFe capped with 30 Å Al, while the film correspond-ing to the lower pattern is thin-ner and consists of 30 Å W and 25 Å CoFe capped with 60 Å Al_2O_3. The lower pattern is vertically shifted for clarity
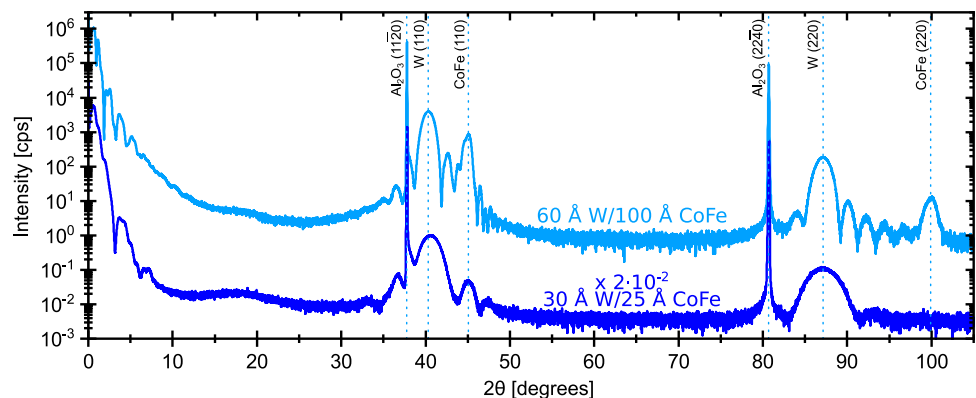
based on the calculation above, if 98 % of the W layer and 92 % of the bilayer are assumed to scatter coherently, then only 88 % of the CoFe layer scatters coherently. As can be observed in Fig. 1c, the relative intensity of the Laue oscillations decreases substantially with a lower degree of coherent scattering. Second, the scattering intensity relates to the form factor and, hence, the atomic number squared Z^2 [76]. Therefore, the scattering intensity from W with $Z = 74$ is expected to be higher by a factor of 7.8 compared to the scattering intensity from the alloy with $Z = 27$ and $Z = 26$ for Co and Fe, respectively.

For the "thin" bilayer sample, only the peak at 45° can be attributed to CoFe. Since its peak position overlaps with the Laue oscillations around the W (110) Bragg peak, a clear identification is difficult. However, the spacing between the peak's position and the Bragg reflection is different compared to the spacing between the Laue oscillations on the lower angle side and the main Bragg reflection, indicating that both do not have the same origin. The intensity of the CoFe (220) Bragg reflection is assumed to lie below the detection limit. However, the presence of a CoFe layer in all samples with finite thickness is confirmed by STEM imaging, results are displayed in Fig. 9a and b.

Due to the limitation of epitaxial growth being reliant on a specific substrate, just like for W, an alternative way of growing epitaxial W/CoFe bilayers was explored

using a single crystalline MgO (001) substrate. To optimize the epitaxial growth, the lattice mismatch between MgO (001)/W (001) with 45° in-plane rotation and between MgO (001)/CoFe were compared. The lattice mismatch between $d_{110} = 2.978$ Å of MgO (001) [51] and $d_{200} = 2.840$ Å of CoFe (001) [16, 74]) is 4.4 %, possibly allowing for epitaxial growth with a 45° in-plane rotated CoFe unit cell. A CoFe (110) growth orientation on MgO (001) is likely to be energetically less favored due to the slightly larger lattice mismatch of 4.5 %. Both mismatches are smaller than the expected mismatch between MgO (001) and W (001) with 45° in-plane rotation of −6.5 %. Therefore, the order of the W and CoFe layers was reversed for the growth on MgO (001) in comparison to the bilayer grown on Al_2O_3 (11$\bar{2}$0).

An x-ray scattering pattern of a 100 Å CoFe/60 Å W bilayer is shown in Fig. 8. Pronounced Kiessig fringes [42] are visible in the small angle regime up until 13° in 2θ, a larger range compared to the bilayer grown on Al_2O_3 (11$\bar{2}$0). Based on the fitting of the reflectivity, the interfaces are flatter compared to the bilayer grown on Al_2O_3 (11$\bar{2}$0). In diffraction, two sharp peaks are observed corresponding to (002) and (004) planes in the MgO (001) substrate. The CoFe (002) Bragg peak is observed in the specular scan at 65.452(6)°, in agreement with the calculated energetically favored [001] growth direction on this substrate. The

Fig. 8 X-ray scattering pattern of a 100 Å CoFe/60 Å W bilayered thin film grown on a single crystalline MgO (001) substrate. The film is capped with 30 Å Al. Indexed peaks relate to the α-W structure
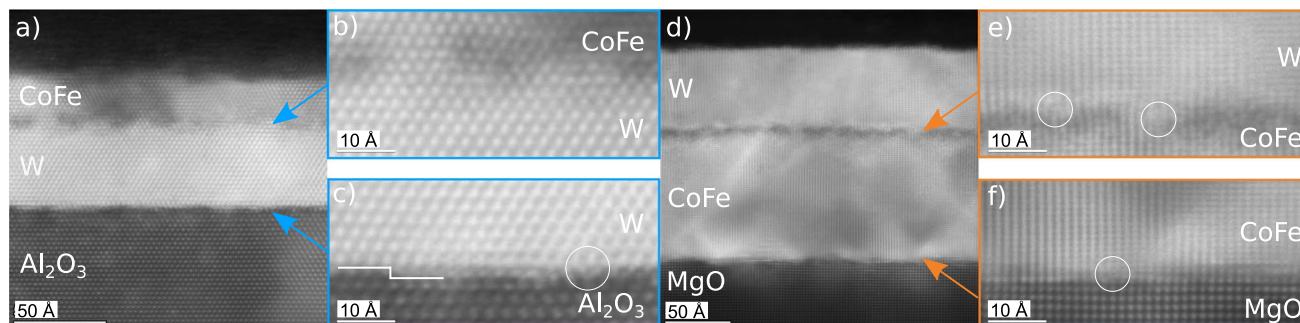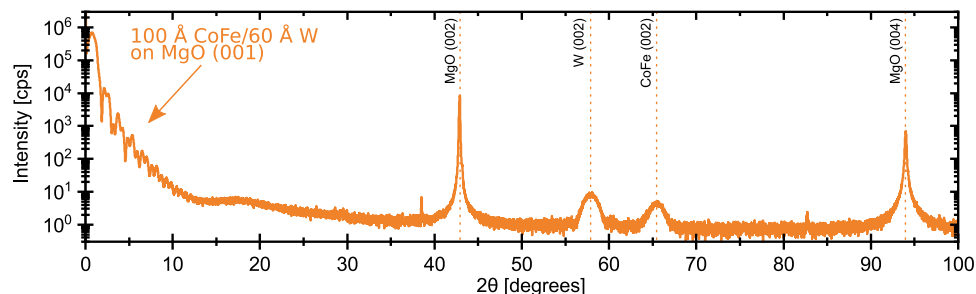

Fig. 9 Cross-section dark field scanning tunneling electron microscopy (STEM) images with high resolution zoom-in of a **a–c** 30 Å W/25 Å CoFe bilayered thin film grown on a single crystalline Al_2O_3 (11$\bar{2}$0) substrate capped with 60 Å Al_2O_3 and a **c–e** 100 Å CoFe/60 Å W bilayered thin film grown on a single crystalline MgO (001) substrate capped with 30 Å Al. Visible defects at the interfaces are marked in white

peak position corresponds to a $d_{002} = 1.425(0)$ Å, which is close to the chemical composition dependent equilibrium value [16, 74, 75]. At 57.905(6)°, a peak is observed which is attributed to W (002). Low intensity Laue oscillations are observed around the W (002) peak indicating epitaxial growth resulting in coherent scattering.

To support the results on crystal structure and epitaxial growth with a real space technique, atomic resolution cross-section STEM images were recorded for bilayers grown on both substrates. A cross-section dark-field STEM image of a W/CoFe bilayer grown on Al_2O_3 (11$\bar{2}$0) is shown in Fig. 9a. The image is recorded of the thin film corresponding to the lower scattering pattern displayed in Fig. 7. High resolution magnifications of the substrate/W and W/CoFe interfaces are displayed in Fig. 9c and b, respectively. Based on the STEM micrographs, the epitaxial growth of W and CoFe layers on Al_2O_3 (11$\bar{2}$0) is confirmed. The atomically sharp boundaries indicate a single-crystalline nature for both layers. Moreover, few misfit dislocations directly at the substrate/film interface are visible as a consequence of large lattice mismatch and strain discussed in detail earlier. In addition, the rather blurry interface for a width of 1–2 monolayers is an indication for relaxation directly at the interface for W grown on this substrate, in agreement with the results of the x-ray scattering and DFT studies. The presence of atomic terraces with a terrace width of a few tens of Ångströms for the Al_2O_3 (11$\bar{2}$0) substrate is confirmed based on these images. Misfit dislocations are also observed at the W/CoFe interface, but the crystal structure of the CoFe layer appears to be single crystalline. Hence, growth with a semicoherent substrate interface of W/CoFe on Al_2O_3 (11$\bar{2}$0) is confirmed.

For comparison, a cross-section dark-field STEM image of a CoFe/W bilayer grown on MgO (001) is shown in Fig. 9d. High resolution magnifications of the substrate/CoFe and CoFe/W interfaces are displayed in Fig. 9f and e, respectively. The images are recorded of the thin film corresponding to the scattering pattern displayed in Fig. 8. The STEM micrographs confirm the epitaxial growth of CoFe/W bilayers on MgO (001), in agreement with the x-ray scattering results. The substrate/CoFe interface seems to be sharp, with strain visible for at least the first 1 to 2 monolayers of CoFe. Dislocations are visible for the CoFe/W interface, however, the W layer itself seems to grow fully single crystalline above the interface.

4 Conclusions

The structural properties of epitaxial α-W thin films deposited on Al_2O_3 (11$\bar{2}$0) and MgO (001) substrates have been studied in in-plane and out-of-plane scattering experiments as well as with real space techniques and electronic transport measurements. Emphasis was given to the overall quality of layering and crystal structure, analyzing the epitaxial relationship and growth mode in combination with *ab initio* calculations. The crystal quality of W (110) on Al_2O_3 (11$\bar{2}$0) was found to be higher compared to films of equivalent thickness on MgO (001) even though the lattice mismatch is larger. The improvement in the crystal quality was attributed to a semicoherent growth mode including the introduction of misfit dislocations directly and in the vicinity of the substrate/film interface, yielding nearly strain-free, highly coherent W layers for thicknesses between 30 and 1000 Å. The degree of relaxation at the interface was, however, found to be highly temperature dependent. Furthermore, the epitaxial growth of W and CoFe bilayers on both substrates was found to be of high crystal quality, exhibiting coherent scattering throughout the total bilayer thickness for W/CoFe films sputtered on Al_2O_3 (11$\bar{2}$0). The results of the extensive x-ray scattering analysis on the epitaxial growth were confirmed by real space high resolution STEM imaging. The detailed analysis of the growth of these epitaxial thin films contributes to an understanding of a mechanism allowing for the high crystal quality, despite a substrate/film lattice mismatch. It is of technological importance, as bilayers of W and CoFe might be essential in future spintronic applications.

Declarations

References

1. A. Hirohata, K. Yamada, Y. Nakatani, I.-L. Prejbeanu, B. Diény, P. Pirro, B. Hillebrands, Review on spintronics: principles and device applications. J. Magn. Magn. Mater. **509**, 166711 (2020). https://doi.org/10.1016/j.jmmm.2020.166711

2. S.S.P. Parkin, Systematic variation of the strength and oscillation period of indirect magnetic exchange coupling through the 3d, 4d, and 5d transition metals. Phys. Rev. Lett. **67**, 3598–3601 (1991). https://doi.org/10.1103/PhysRevLett.67.3598

3. H. Liu, A. Ciuciulkaite, V. Kapaklis, D. Karaiskaj, D.A. Arena, Enhanced optical mode coherence in exchange coupled soft magnetic multilayers. J. Appl. Phys. **131**, 213902 (2022). https://doi.org/10.1063/5.0093827. (**and references therein**)

4. C.-F. Pai, L. Liu, Y. Li, H.W. Tseng, D.C. Ralph, R.A. Buhrman, Spin transfer torque devices utilizing the giant spin Hall effect of tungsten. Appl. Phys. Lett. **101**, 122404 (2012). https://doi.org/10.1063/1.4753947

5. Y. Tserkovnyak, A. Brataas, G.E.W. Bauer, Enhanced gilbert damping in thin ferromagnetic films. Phys. Rev. Lett. **88**, 117601 (2002). https://doi.org/10.1103/PhysRevLett.88.117601

6. R.A. Causey, T.J. Venhaus, The use of tungsten in fusion reactors: a review of the hydrogen retention and migration properties. Phys. Scr. **2001**(T94), 9 (2001). https://doi.org/10.1238/Physica.Topical.094a00009

7. M. Kaufmann, R. Neu, Tungsten as first wall material in fusion devices. Fusion Eng. Des. **82**(5), 521–527 (2007). In: Proceedings of the 24th Symposium on Fusion Technology. https://doi.org/10.1016/j.fusengdes.2007.03.045

8. M.J. O'Keefe, J.T. Grant, Phase transformation of sputter deposited tungsten thin films with A-15 structure. J. Appl. Phys. **79**(12), 9134–9141 (1996). https://doi.org/10.1063/1.362584

9. Q. Hao, G. Xiao, Giant spin hall effect and switching induced by spin-transfer torque in a W/Co40Fe40B20/MgO structure with perpendicular magnetic anisotropy. Phys. Rev. Appl. **3**, 034009 (2015). https://doi.org/10.1103/physrevapplied.3.034009

10. Q. Hao, W. Chen, G. Xiao, Beta (β) tungsten thin films: structure, electron transport, and giant spin Hall effect. Appl. Phys. Lett. **106**(18), 182403 (2015). https://doi.org/10.1063/1.4919867

11. W. Chen, L. Qian, G. Xiao, Deterministic current induced magnetic switching without external field using Giant Spin Hall Effect of β-W. Sci. Rep. **8**(1), 8144 (2018). https://doi.org/10.1038/s41598-018-26586-z

12. Y.G. Shen, Y.W. Mai, Q.C. Zhang, D.R. McKenzie, W.D. McFall, W.E. McBride, Residual stress, microstructure, and structure of tungsten thin films deposited by magnetron sputtering. J. Appl. Phys. **87**(1), 177–187 (2000). https://doi.org/10.1063/1.371841

13. F.T.N. Vüllers, R. Spolenak, Alpha- vs. beta-W nanocrystalline thin films: a comprehensive study of sputter parameters and resulting materials' properties. Thin Solid Films **577**, 26–34 (2015). https://doi.org/10.1016/j.tsf.2015.01.030

14. S.M. Rossnagel, I.C. Noyan, J.C. Cabral, Phase transformation of thin sputter-deposited tungsten films at room temperature. J Vacuum Sci Technol B Microelectron Nanometer Struct Process Measur Phenom **20**(5), 2047–2051 (2002). https://doi.org/10.1116/1.1506905

15. W.P. Davey, The lattice parameter and density of pure tungsten. Phys. Rev. **26**, 736–738 (1925). https://doi.org/10.1103/PhysRev.26.736

16. A. Jain, S.P. Ong, G. Hautier, W. Chen, W.D. Richards, S. Dacek, S. Cholia, D. Gunter, D. Skinner, G. Ceder, K.A. Persson, Commentary: the materials project: a materials genome approach to accelerating materials innovation. APL Mater. **1**(1), 011002 (2013). https://doi.org/10.1063/1.4812323

17. Materials Data on W by Materials Project. The Materials Project (2020). https://doi.org/10.17188/1312984

18. D. Thonig, Tcv Rauch, H. Mirhosseini, J. Henk, I. Mertig, H. Wortelen, B. Engelkamp, A.B. Schmidt, M. Donath, Existence of topological nontrivial surface states in strained transition metals: W, ta, mo, and nb. Phys. Rev. B **94**, 155132 (2016). https://doi.org/10.1103/PhysRevB.94.155132

19. G. Song, A. Remhof, K. Theis-Bröhl, H. Zabel, Extraordinary adhesion of niobium on sapphire substrates. Phys. Rev. Lett. **79**, 5062–5065 (1997). https://doi.org/10.1103/PhysRevLett.79.5062

20. A.R. Wildes, J. Mayer, K. Theis-Bröhl, The growth and structure of epitaxial niobium on sapphire. Thin Solid Films **401**(1), 7–34 (2001). https://doi.org/10.1016/S0040-6090(01)01631-5

21. C. Bull, S.M. Hewett, R. Ji, C.-H. Lin, T. Thomson, D.M. Graham, P.W. Nutter, Spintronic terahertz emitters: Status and prospects from a materials perspective. APL Mater. **9**, 090701 (2021)

22. M. Björck, G. Andersson, GenX: an extensible X-ray reflectivity refinement program utilizing differential evolution. J. Appl. Crystallogr. **40**(6), 1174–1178 (2007). https://doi.org/10.1107/S0021889807045086

23. A. Glavic, M. Björck, GenX 3: the latest generation of an established tool. J. Appl. Crystallogr. **55**(4), 1063–1071 (2022). https://doi.org/10.1107/S1600576722006653

24. M. Yoshimoto, T. Maeda, T. Ohnishi, H. Koinuma, O. Ishiyama, M. Shinohara, M. Kubo, R. Miura, A. Miyamoto, Atomic-scale formation of ultrasmooth surfaces on sapphire substrates for high-quality thin-film fabrication. Appl. Phys. Lett. **67**(18), 2615–2617 (1995). https://doi.org/10.1063/1.114313

25. J.L. Schroeder, A.S. Ingason, J. Rosén, J. Birch, Beware of poor-quality MgO substrates: a study of MgO substrate quality and its effect on thin film quality. J. Cryst. Growth **420**, 22–31 (2015). https://doi.org/10.1016/j.jcrysgro.2015.03.010

26. Ravensburg, A.L., Bylin, J., Pálsson, G.K., Kapaklis, V.: GENL: An extensible fitting program for Laue oscillations. arXiv e-prints, 2310–13539 (2023) https://doi.org/10.48550/arXiv.2310.13539arXiv:2310.13539 [cond-mat.mtrl-sci]

27. L.J. van der Pauw, A method of measuring specific resistivity and hall effect of discs of arbitrary shape. Philips Res. Rep. **13**(1), 1–9 (1958)

28. V. Garcia-Vazquez, N. Perez-Amaro, A. Canizo-Cabrera, B. Cumplido-Espindola, R. Martinez-Hernandez, M.A. Abarca-Ramirez, Selected error sources in resistance measurements on superconductors. Rev. Sci. Instrum. **72**(July 2001), 3332 (2001). https://doi.org/10.1063/1.1386899

29. P. Hohenberg, W. Kohn, Inhomogeneous electron gas. Phys. Rev. **136**, 864–871 (1964). https://doi.org/10.1103/PhysRev.136.B864

30. G. Kresse, J. Hafner, Ab initio molecular dynamics for open-shell transition metals. Phys. Rev. B **48**, 13115–13118 (1993). https://doi.org/10.1103/PhysRevB.48.13115

31. G. Kresse, J. Hafner, Ab initio molecular-dynamics simulation of the liquid-metal-amorphous-semiconductor transition in germanium. Phys. Rev. B **49**, 14251–14269 (1994). https://doi.org/10.1103/PhysRevB.49.14251

32. G. Kresse, D. Joubert, From ultrasoft pseudopotentials to the projector augmented-wave method. Phys. Rev. B **59**, 1758–1775 (1999). https://doi.org/10.1103/PhysRevB.59.1758

33. J.P. Perdew, K. Burke, M. Ernzerhof, Generalized gradient approximation made simple. Phys. Rev. Lett. **77**, 3865–3868 (1996). https://doi.org/10.1103/PhysRevLett.77.3865

34. P.E. Blöchl, Projector augmented-wave method. Phys. Rev. B **50**, 17953–17979 (1994). https://doi.org/10.1103/PhysRevB.50.17953

35. H.J. Monkhorst, J.D. Pack, Special points for Brillouin-zone integrations. Phys. Rev. B **13**, 5188–5192 (1976). https://doi.org/10.1103/PhysRevB.13.5188

36. D.P. Sigumonrong, J. Zhang, Y. Zhou, D. Music, J. Emmerlich, J. Mayer, J.M. Schneider, Interfacial structure of V_2AlC thin films deposited on (11$\bar{2}$0)-sapphire. Scripta Mater. **64**(4), 347–350 (2011). https://doi.org/10.1016/j.scriptamat.2010.10.035

37. J. Mayer, J.A. Dura, C.P. Flynn, M. Rühle, Electron microscopy studies of Nb-Al_2O_3 interfaces formed by molecular beam epitaxy. Surf. Coat. Technol. **43–44**, 199–212 (1990). https://doi.org/10.1016/0257-8972(90)90074-M

38. J. Mayer, G. Gutekunst, G. Möbus, J. Dura, C.P. Flynn, M. Rühle, Structure and defects of MBE grown NbAl$_2$O$_3$ interfaces. Acta Metallur. Mater. **40**, 217–225 (1992). https://doi.org/10.1016/0956-7151(92)90280-R

39. J. Guo, D.E. Ellis, D.J. Lam, Electronic structure and energetics of sapphire (0001) and (11$\bar{}$02) surfaces. Phys. Rev. B **45**, 13647–13656 (1992) https://doi.org/10.1103/PhysRevB.45.13647

40. S. Blonski, S.H. Garofalini, Molecular dynamics simulations of alpha-alumina and gamma-alumina surfaces. Surf. Sci. **295**(1), 263–274 (1993). https://doi.org/10.1016/0039-6028(93)90202-U

41. Z. Lin, P.D. Bristowe, Microscopic characteristics of the Ag(111)/ZnO(0001) interface present in optical coatings. Phys. Rev. B **75**, 205423 (2007). https://doi.org/10.1103/PhysRevB.75.205423

42. H. Kiessig, Untersuchungen zur Totalreflexion von Röntgenstrahlen. Ann. Phys. **402**(6), 715–768 (1931). https://doi.org/10.1002/andp.19314020607

43. H. Park, D.-H. Han, H.T. Lim, W. Choi, H.J. Kim, First-principles investigation of morphological evolution of tungsten growth on alumina surfaces: implications for thin-film growth. ACS Appl. Nano Mater. **5**(11), 16365–16375 (2022). https://doi.org/10.1021/acsanm.2c03414

44. P. Petroff, T.T. Sheng, A.K. Sinha, G.A. Rozgonyi, F.B. Alexander, Microstructure, growth, resistivity, and stresses in thin tungsten films deposited by rf sputtering. J. Appl. Phys. **44**(6), 2545–2554 (1973). https://doi.org/10.1063/1.1662611

45. M.J. O'Keefe, J.T. Grant, Phase transformation of sputter deposited tungsten thin films with A-15 structure. J. Appl. Phys. **79**(12), 9134–9141 (1996). https://doi.org/10.1063/1.362584

46. M.X. Liu, Y.L. Huang, F. Ma, K.W. Xu, Template-induced formation of α-W and size-dependent properties of tungsten thin films. Mater. Sci. Eng. B **139**(1), 99–104 (2007). https://doi.org/10.1016/j.mseb.2007.01.042

47. H. Park, D.-H. Han, H.T. Lim, W. Choi, H.J. Kim, First-principles investigation of morphological evolution of tungsten growth on alumina surfaces: implications for thin-film growth. ACS Appl. Nano Mater. **5**(11), 16365–16375 (2022). https://doi.org/10.1021/acsanm.2c03414

48. A.J. Lee, J.T. Brangham, Y. Cheng, S.P. White, W.T. Ruane, B.D. Esser, D.W. McComb, P.C. Hammel, F. Yang, Metallic ferromagnetic films with magnetic damping under 1.4 x 10^{-3}. Nat. Commun. **8**(1), 234 (2017). https://doi.org/10.1038/s41467-017-00332-x

49. A.L. Ravensburg, G.K. Pálsson, M. Pohlit, B. Hjörvarsson, V. Kapaklis, Influence of misfit strain on the physical properties of Fe thin films. Thin Solid Films **761**, 139494 (2022). https://doi.org/10.1016/j.tsf.2022.139494

50. O.F.K. McGrath, F. Robaut, N. Cherief, A. Liénard, M. Brunel, D. Givord, Epitaxial growth of W(110) on Al_2O_3(11$\bar{2}$0) by pulsed laser deposition. Surf. Sci. **315**(3), 1017–1020 (1994). https://doi.org/10.1016/0039-6028(94)90124-4

51. P. Zheng, B.D. Ozsdolay, D. Gall, Epitaxial growth of tungsten layers on MgO(001). J. Vacuum Sci. Technol. A **33**(6), 10 (2015). https://doi.org/10.1116/1.4928409

52. B. Wölfing, K. Theis-Bröhl, C. Sutter, H. Zabel, Afm and x-ray studies on the growth and quality of nb(110) on. J. Phys. Condens. Matter **11**(13), 2669 (1999). https://doi.org/10.1088/0953-8984/11/13/004

53. J.H. Souk, A. Segmüller, J. Angilello, Oriented growth of ultrathin tungsten films on sapphire substrates. J. Appl. Phys. **62**(2), 509–512 (1987). https://doi.org/10.1063/1.339775

54. J. Mayer, C.P. Flynn, M. Rühle, High-resolution electron microscopy studies of Nb/Al_2O_3 interfaces. Ultramicroscopy **33**(1), 51–61 (1990). https://doi.org/10.1016/0304-3991(90)90104-T

55. Materials data on Al_2O_3 by materials project. The Materials Project (2020) https://doi.org/10.17188/1187823

56. P.O. Renault, K.F. Badawi, L. Bimbault, P. Goudeau, E. Elkaim, J.P. Lauriat, Poisson's ratio measurement in tungsten thin films combining an x-ray diffractometer with in situ tensile tester. Appl. Phys. Lett. **73**(14), 1952–1954 (1998). https://doi.org/10.1063/1.122332

57. A.J. Ying, C.E. Murray, I.C. Noyan, A rigorous comparison of x-ray diffraction thickness measurement techniques using silicon-on-insulator thin films. J. Appl. Crystallogr. **42**(3), 401–410 (2009). https://doi.org/10.1107/S0021889809006888

58. J.-Y. Cheng, M.K.Y. Chan, C.M. Lilley, Enabling direct silicene integration in electronics: first principles study of silicene on NiSi2(111). Appl. Phys. Lett. **109**(13), 133111 (2016). https://doi.org/10.1063/1.4963653

59. C. Kruse, First-principles study of the atomistic and electronic structure of the niobium-alumina (0001) interface. Philos. Mag. Lett. **73**(6), 377–384 (1996). https://doi.org/10.1080/095008396180650

60. I.G. Batirev, A. Alavi, M.W. Finnis, T. Deutsch, First-principles calculations of the ideal cleavage energy of bulk niobium(111)/α-alumina(0001) interfaces. Phys. Rev. Lett. **82**, 1510–1513 (1999). https://doi.org/10.1103/PhysRevLett.82.1510

61. F. Herrig, D. Music, B. Völker, M. Hans, P.J. Pöllmann, A.L. Ravensburg, J.M. Schneider, Ab initio guided low temperature synthesis strategy for smooth face-centred cubic femn thin films. Metals **8**(6), 384 (2018). https://doi.org/10.3390/met8060384

62. D. Choi, C.S. Kim, D. Naveh, S. Chung, A.P. Warren, N.T. Nuhfer, M.F. Toney, K.R. Coffey, K. Barmak, Electron mean free path of tungsten and the electrical resistivity of epitaxial (110) tungsten films. Phys. Rev. B **86**(4), 045432 (2012). https://doi.org/10.1103/physrevb.86.045432

63. V. Frank, Hall coefficient of technically pure metals from 80 K to 800 K. Appl. Sci. Res. Sect. B **6**(1), 379–387 (1957). https://doi.org/10.1007/bf02920394

64. C.M. Hurd, *The Hall Effect in Metals and Alloys*, 1st edn. (Springer, New York, 1972). https://doi.org/10.1007/978-1-4757-0465-5

65. N.V. Volkenshtein, V.N. Kachinskii, L.S. Starostina, The Fermi Surface of Tungsten. Soviet Phys. JETP **18**(1), 32–33 (1964)

66. W.W. Schulz, P.B. Allen, N. Trivedi, Hall coefficient of cubic metals. Phys. Rev. B **45**(19), 10886–10890 (1992). https://doi.org/10.1103/physrevb.45.10886

67. O.A. Panchenko, P.P. Lutsishin, Y.G. Ptushinskii, Galvanomagnetic effects in thin films of some transition metals. Soviet Phys. JETP **29**(1), 76–78 (1969)

68. Z. Bastl, The Hall effect in tungsten films influenced by hydrogen chemisorption. Thin Solid Films **10**(2), 311–313 (1972). https://doi.org/10.1016/0040-6090(72)90198-8

69. J.L. Vassent, M. Dynna, A. Marty, B. Gilles, G. Patrat, A study of growth and the relaxation of elastic strain in MgO on Fe(001). J. Appl. Phys. **80**(10), 5727–5735 (1996). https://doi.org/10.1063/1.363626

70. H.L. Meyerheim, R. Popescu, J. Kirschner, N. Jedrecy, M. Sauvage-Simkin, B. Heinrich, R. Pinchaux, Geometrical and compositional structure at metal-oxide interfaces: MgO on Fe(001). Phys. Rev. Lett. **87**, 076102 (2001). https://doi.org/10.1103/PhysRevLett.87.076102

71. H.L. Meyerheim, R. Popescu, N. Jedrecy, M. Vedpathak, M. Sauvage-Simkin, R. Pinchaux, B. Heinrich, J. Kirschner, Surface x-ray diffraction analysis of the MgO/Fe(001) interface: evidence for an FeO layer. Phys. Rev. B **65**, 144433 (2002). https://doi.org/10.1103/PhysRevB.65.144433

72. T. Devolder, T. Tahmasebi, S. Eimer, T. Hauet, S. Andrieu, Compositional dependence of the magnetic properties of epitaxial FeV/MgO thin films. Appl. Phys. Lett. **103**(24), 242410 (2013). https://doi.org/10.1063/1.4845375

73. P. Scherrer, Estimation of the size and internal structure of colloidal particles by means of Röntgen. Nachr. Ges. Wiss. Göttingen **2**, 96–100 (1918)

74. Materials Data on FeCo by Materials Project. The Materials Project (2020) https://doi.org/10.17188/1196095

75. A.Y. Liu, D.J. Singh, General-potential study of the electronic and magnetic structure of FeCo. Phys. Rev. B **46**, 11145–11148 (1992). https://doi.org/10.1103/PhysRevB.46.11145

76. P.F. Fewster, X-ray analysis of thin films and multilayers. Rep. Prog. Phys. **59**(11), 1339–1407 (1996). https://doi.org/10.1088/0034-4885/59/11/001